Energy dependence of Λ and Ξ production in central Pb+Pb collisions at 20A, 30A, 40A, 80A, and 158A GeV measured at the CERN Super Proton Synchrotron

C. Alt,[9] T. Anticic,[23] B. Baatar,[8] D. Barna,[4] J. Bartke,[6] L. Betev,[10] H. Białkowska,[20] C. Blume,[9] B. Boimska,[20] M. Botje,[1] J. Bracinik,[3] R. Bramm,[9] P. Buncic,[10] V. Cerny,[3] P. Christakoglou,[2] P. Chung,[19] O. Chvala,[14] J.G. Cramer,[16] P. Csató,[4] P. Dinkelaker,[9] V. Eckardt,[13] D. Flierl,[9] Z. Fodor,[4] P. Foka,[7] V. Friese,[7] J. Gál,[4] M. Gaździcki,[9,11] V. Genchev,[18] E. Gładysz,[6] K. Grebieszkow,[22] S. Hegyi,[4] C. Höhne,[7] K. Kadija,[23] A. Karev,[13] D. Kikola,[22] M. Kliemant,[9] S. Kniege,[9] V.I. Kolesnikov,[8] E. Kornas,[6] M. Kowalski,[6] I. Kraus,[7] M. Kreps,[3] A. Laszlo,[4] R. Lacey,[19] M. van Leeuwen,[1] P. Lévai,[4] L. Litov,[17] B. Lungwitz,[9] M. Makariev,[17] A.I. Malakhov,[8] M. Mateev,[17] G.L. Melkumov,[8] C. Meurer,[9] A. Mischke,[1] M. Mitrovski,[9] J. Molnár,[4] St. Mrówczyński,[11] V. Nicolic,[23] G. Pálla,[4] A.D. Panagiotou,[2] D. Panayotov,[17] A. Petridis,[2,*] W. Peryt,[22] M. Pikna,[3] J. Pluta,[22] D. Prindle,[16] F. Pühlhofer,[12] R. Renfordt,[9] A. Richard,[9] C. Roland,[5] G. Roland,[5] M. Rybczyński,[11] A. Rybicki,[6] A. Sandoval,[7] N. Schmitz,[13] T. Schuster,[9] P. Seyboth,[13] F. Siklér,[4] B. Sitar,[3] E. Skrzypczak,[21] M. Slodkowski,[22] G. Stefanek,[11] R. Stock,[9] C. Strabel,[9] H. Ströbele,[9] T. Susa,[23] I. Szentpétery,[4] J. Sziklai,[4] M. Szuba,[22] P. Szymanski,[10,20] V. Trubnikov,[20] M. Utvić,[9] D. Varga,[4,10] M. Vassiliou,[2] G.I. Veres,[4,5] G. Vesztergombi,[4] D. Vranić,[7] A. Wetzler,[9] Z. Włodarczyk,[11] A. Wojtaszek,[11] I.K. Yoo,[15] and J. Zimányi[4,*]

(The NA49 Collaboration)

[1] *NIKHEF, Amsterdam, Netherlands.*
[2] *Department of Physics, University of Athens, Athens, Greece.*
[3] *Comenius University, Bratislava, Slovakia.*
[4] *KFKI Research Institute for Particle and Nuclear Physics, Budapest, Hungary.*
[5] *MIT, Cambridge, USA.*
[6] *Henryk Niewodniczanski Institute of Nuclear Physics, Polish Academy of Sciences, Cracow, Poland.*
[7] *Gesellschaft für Schwerionenforschung (GSI), Darmstadt, Germany.*
[8] *Joint Institute for Nuclear Research, Dubna, Russia.*
[9] *Fachbereich Physik der Universität, Frankfurt, Germany.*
[10] *CERN, Geneva, Switzerland.*
[11] *Institute of Physics Świętokrzyska Academy, Kielce, Poland.*
[12] *Fachbereich Physik der Universität, Marburg, Germany.*
[13] *Max-Planck-Institut für Physik, Munich, Germany.*
[14] *Charles University, Faculty of Mathematics and Physics, Institute of Particle and Nuclear Physics, Prague, Czech Republic.*
[15] *Department of Physics, Pusan National University, Pusan, Republic of Korea.*
[16] *Nuclear Physics Laboratory, University of Washington, Seattle, WA, USA.*
[17] *Atomic Physics Department, Sofia University St. Kliment Ohridski, Sofia, Bulgaria.*
[18] *Institute for Nuclear Research and Nuclear Energy, Sofia, Bulgaria.*
[19] *Department of Chemistry, Stony Brook Univ. (SUNYSB), Stony Brook, USA.*
[20] *Institute for Nuclear Studies, Warsaw, Poland.*
[21] *Institute for Experimental Physics, University of Warsaw, Warsaw, Poland.*
[22] *Faculty of Physics, Warsaw University of Technology, Warsaw, Poland.*
[23] *Rudjer Boskovic Institute, Zagreb, Croatia.*

Results on Λ, $\bar{\Lambda}$, Ξ^-, and $\bar{\Xi}^+$ production in central Pb+Pb reactions at 20A, 30A, 40A, 80A, and 158A GeV are presented. The energy dependence of transverse mass spectra, rapidity spectra, and multiplicities is discussed. Comparisons to string hadronic models (UrQMD and HSD) and statistical hadron gas models are shown. While the latter provide a reasonable description of all particle yields, the first class of models fails to match the Ξ^- and $\bar{\Xi}^+$ multiplicities.

I. INTRODUCTION

Heavy ion reactions at ultra-relativistic energies allow the study of strongly interacting matter at extreme temperatures and densities. It is expected that under such conditions eventually a quark gluon plasma (QGP) will be formed. In this state of matter the normal confinement of quarks and gluons in hadrons is removed and the partons can exist as quasi-free particles in an extended region of space-time. One of the first signatures proposed for the formation of a QGP state was an enhancement of strange particle production in A+A with respect to p+p collisions [1]. The argumentation relies on the assumption that gluon fusion processes, which may be dominant in a QGP, produce additional $s\bar{s}$ pairs[2]. This in turn will cause the abundance of strange quarks to reach its chemical equilibrium value in much shorter times than

[*] deceased

would be possible in a pure hadronic scenario. In fact, the enhanced production of strange particles has been observed already quite early in high energy nucleus–nucleus collisions [3, 4]. It has also been demonstrated that the enhancement is most pronounced for the multiply strange hyperons Ξ and Ω [5, 6, 7].

However, systematic studies of hadron production in nucleus–nucleus collisions have shown that strangeness enhancement is not only seen at high energies, such as top SPS and RHIC energies, but it is also observed at lower energies ($\sqrt{s_{\rm NN}} < 5$ GeV) [8] where no QGP formation is expected. Actually, here the production of Λ and Ξ exhibits an even stronger enhancement than present at top SPS or RHIC energies [9, 10, 11]. Generally, it is found that the abundances of strange particles in central A+A reactions are similar to those expected from statistical hadron gas models assuming a grand canonical ensemble [12, 13]. While the enhancement at lower energies can to a certain extent also be explained by transport models, at higher energies additional mechanisms have to be involved in order to reach chemical equilibrium values via a dynamical evolution. It has, e.g., been suggested that multi-pion reaction processes can lead to an accelerated equilibration of anti-hyperon production in nucleus–nucleus collisions [14]. Especially at larger densities, as present close to the QGP phase boundary, processes like this might drive the system quite fast to a chemical equilibrium state [15]. Still it is an open question whether such dynamical explanations are applicable as well at lower energies. On the other hand, it was suggested that particle production via strong interaction always follows the maximum entropy principle and therefore hadron abundances are naturally close to the outcome of statistical processes [16, 17, 18, 19]. The measurement of hyperon production in an energy range below top SPS energy ($\sqrt{s_{\rm NN}} < 17.3$ GeV) provides important constraints on both, the statistical and transport model approach. Recent results on kaon production in central nucleus–nucleus collisions [20] indicate a sharp maximum of the ratio $\langle {\rm K}^+\rangle/\langle\pi^+\rangle$ and a sudden change in the energy dependence of the $\langle m_{\rm t}\rangle - m_0$ of pions, kaons, and protons at a beam energy of 30A GeV, where $m_{\rm t} = \sqrt{p_{\rm t}^2 + m_0^2}$ is the transverse mass, m_0 the rest mass and $p_{\rm t}$ the transverse momentum. These anomalies can be interpreted as a signal for the onset of deconfinement [21, 22] and might also be visible in the energy dependence of hyperon yields.

The data discussed here represent an extension of previously published results [10, 11, 23] in order to provide a complete study of the energy dependence of hyperon production at the CERN-SPS. Some of the data discussed here have been presented as preliminary before [7, 24, 25]. However, the data shown in this publication are the result of a completely new and independent analysis, which treats all datasets in a consistent manner. In particular, the results for Λ and $\bar{\Lambda}$ include a correction for the feeddown from weak decays, which was not applied in the previous publication [10].

TABLE I: Summary of the analyzed datasets. The centrality fraction corresponds to the most central part of the total inelastic cross section. The Glauber model was used to determine the averaged number of wounded nucleons per event $\langle N_{\rm w}\rangle$.

$E_{\rm beam}$ (A GeV)	$\sqrt{s_{\rm NN}}$ (GeV)	$y_{\rm cm}$	Cent. (%)	$\langle N_{\rm w}\rangle$	Year	Statistics
20	6.3	1.88	7	349	2002	350k
30	7.6	2.08	7	349	2002	420k
40	8.7	2.22	7	349	1999	380k(Λ)/580k(Ξ)
80	12.3	2.56	7	349	2000	300k
158	17.3	2.91	10	335	2000	1.2M

II. DATA ANALYSIS

A. Experimental setup and data sets

The data were taken with the NA49 large acceptance hadron spectrometer at the CERN SPS. A detailed description of the apparatus can be found in [26]. With this detector, tracking is performed by four large-volume Time Projection Chambers (TPCs) in a wide range of phase space. Two of these are positioned inside two superconducting dipole magnets. In order to assure a similar detector acceptance for all datasets, the magnetic field was chosen proportional to the beam energy. A measurement of the specific energy loss ${\rm d}E/{\rm d}x$ in the TPC gas with a typical resolution of 4% provides particle identification at forward rapidities. Time-of-flight detectors improve the particle identification at mid-rapidity. Central Pb+Pb reactions were selected by imposing an upper threshold on the energy measured in the projectile fragmentation region. For this measurement the Zero Degree Calorimeter (ZDC) was used which is positioned downstream of the TPCs. A collimator in front of the ZDC assures that the acceptance of the calorimeter matches the phase space of the projectile fragments and spectator nucleons.

We present in this paper an analysis of central Pb+Pb events taken at beam energies of 20A, 30A, 40A, 80A, and 158A GeV in the years between 1999 – 2002. The properties of the different datasets are summarized in Table I. The 158A GeV dataset has an online centrality trigger on the 23.5% most central events, of which the 10% most central were selected offline.

B. Λ ($\bar{\Lambda}$) and Ξ^- ($\bar{\Xi}^+$) reconstruction

Λ and $\bar{\Lambda}$ hyperons were found by reconstructing their charged decays $\Lambda \to \pi^- + {\rm p}$ and $\bar{\Lambda} \to \pi^+ + \bar{\rm p}$ (branching ratio 63.9 % [27]). In a first step pairs were formed of all positively charged particles with all negatively charged ones. Their tracks were reconstructed by a global tracking algorithm that connects the track parts registered

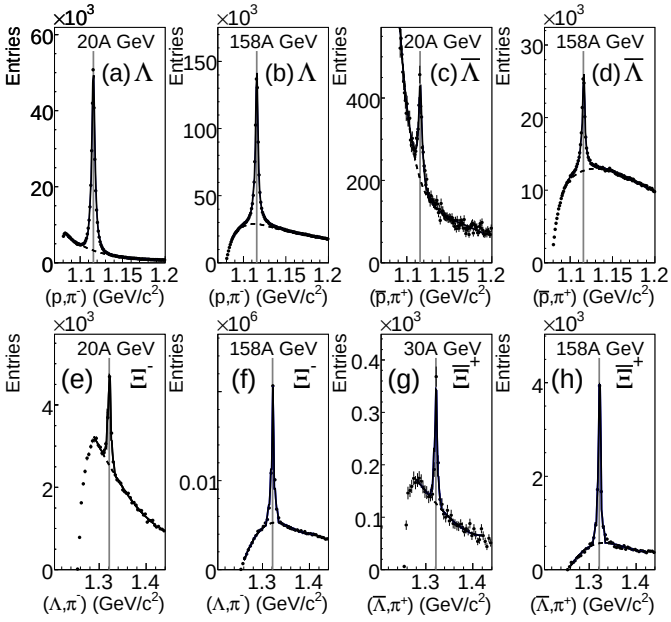

FIG. 1: The invariant mass distributions of all Λ, $\bar{\Lambda}$ (upper row), Ξ^-, and $\bar{\Xi}^+$ (lower row) candidates in central Pb+Pb collisions at the lowest and highest analyzed beam energies. The full curves represent a fit to signal and background as described in the text, while the dashed curves show the background contribution only. The gray vertical lines denote the PDG masses [27].

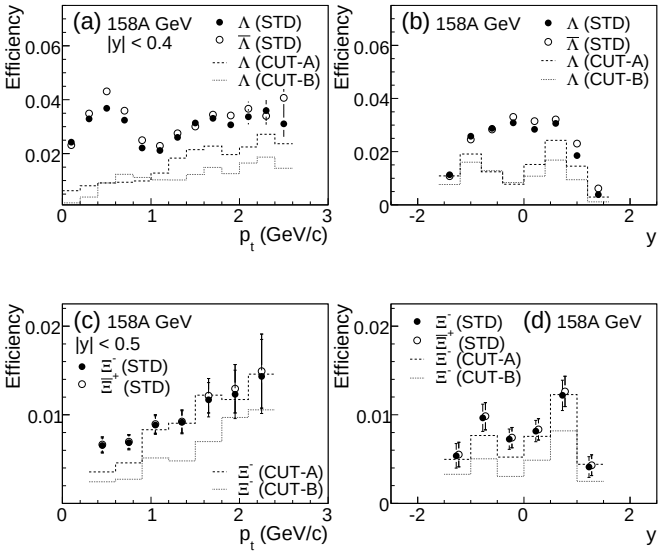

FIG. 2: The total reconstruction efficiency of Λ ($\bar{\Lambda}$) (upper row) and Ξ^- ($\bar{\Xi}^+$) (lower row) as a function of $p_{\rm t}$ (left panels), and as a function of rapidity (right panels) for central Pb+Pb at 158A GeV. The symbols denote the efficiency for the standard analysis procedure (STD). In addition, the Λ (Ξ^-) efficiencies for two other selection criteria are shown (dashed: CUT-A, dotted: CUT-B, see text).

in the different TPCs. Only tracks with more than 10 reconstructed points were accepted. By requiring a distance of closest approach (DCA) between their trajectories of less than 0.5 cm anywhere between the position of the first measured points on the tracks and the target plane, V^0 candidates were identified. A set of additional cuts was imposed in order to reduce the combinatorial background due to uncorrelated pairs. Identification of (anti-)protons via their specific energy loss ($\mathrm{d}E/\mathrm{d}x$) in the TPCs reduces the contribution of pairs with a wrong mass assignment. The measured $\mathrm{d}E/\mathrm{d}x$ was required to be within 3.5 standard deviations from the predicted Bethe-Bloch value. A Λ ($\bar{\Lambda}$) candidate was accepted if the reconstructed position of its decay vertex is at least 30 cm downstream from the target and outside the sensitive volume of the TPCs, to avoid inefficiencies resulting from an insufficient separation of the clusters of the two tracks. The trajectories of the Λ ($\bar{\Lambda}$) candidates were extrapolated back to the target plane to determine their impact parameters $b_{\rm x}$ (in the magnetic bending plane) and $b_{\rm y}$ relative to the interaction point. Non-vertex candidates were rejected by requiring $|b_{\rm x}| < 0.5$ cm and $|b_{\rm y}| < 0.25$ cm. A further reduction of the combinatorial background was achieved by placing a requirement on the angle θ^* between the flight direction of the mother particle and of its positive daughter, determined in the center-of-mass system of the Λ ($\bar{\Lambda}$) candidate: $-0.95 < \cos\theta^* < 0.75$. Figure 1, upper row, shows as examples the resulting invariant mass spectra at 20A and 158A GeV for Λ and $\bar{\Lambda}$. The position of the peaks in the $m_{\rm inv}$ distribution agrees with the nominal Λ mass determined by the particle data group [27]. From a fit with a Gaussian typical mass resolutions of $\sigma_{\rm m} \approx 2$ MeV/c^2 are determined, which depend only slightly on phase space and beam energy. Generally, the signal to background ratio (S/B) is worse for $\bar{\Lambda}$ than for Λ, due to the lower yield of real $\bar{\Lambda}$. While S/B decreases with energy for Λ, it is constant for $\bar{\Lambda}$. However, the shape of the combinatorial background depends on beam energy in both cases.

Ξ^- ($\bar{\Xi}^+$) candidates were identified via the decay channel $\Xi^- \to \Lambda + \pi^-$ ($\bar{\Xi}^+ \to \bar{\Lambda} + \pi^+$) which has a branching ratio of 99.9 % [27]. To reconstruct the Ξ^- ($\bar{\Xi}^+$), Λ ($\bar{\Lambda}$) candidates were selected in an invariant mass window of 1.101 – 1.131 GeV/c^2 and combined with all measured negatively (positively) charged particles in the event. The Λ ($\bar{\Lambda}$) candidates were required to pass the same cuts as described above, with the exception of the cuts on $b_{\rm x/y}$ and $\cos\theta^*$, which were not applied here. The reconstructed Ξ^- ($\bar{\Xi}^+$) candidates should point back to the interaction vertex, while the pions from Λ ($\bar{\Lambda}$) and the Ξ^- ($\bar{\Xi}^+$) decay will on average have a larger impact parameter. To reject non-vertex candidates, upper limits of $|b_{\rm x}| < 0.5$ cm and $|b_{\rm y}| < 0.25$ cm were therefore imposed on the Ξ^- ($\bar{\Xi}^+$) candidates. Pions coming from the primary interaction point were removed by a cut of $|b_{\rm y}| > 1.0$ cm for the negatively (positively) charged tracks associated to the Ξ^- ($\bar{\Xi}^+$) decay ver-

tex and $|b_y| > 0.5$ cm for the negatively (positively) charged daughter tracks of the Λ ($\bar{\Lambda}$) candidates. An additional improvement of the signal to background ratio was achieved by requiring that the Λ decay vertex and the pion track were measured on the same side of the TPCs relative to the beam pipe. The lowest beam energy where a significant $\bar{\Xi}^+$ signal could be extracted is 30A GeV, while Ξ^- could be analyzed at all available energies. Figure 1, lower row, shows the invariant mass distributions for Ξ^- and $\bar{\Xi}^+$ candidates after all selection criteria at the lowest and highest available energies, respectively. Similarly as in the case of the Λ ($\bar{\Lambda}$) an excellent agreement of the peak positions with the PDG masses [27] is observed. The typical mass resolution, as obtained from a fit with a Gaussian is $\sigma_m \approx 4$ MeV/c^2. The dependence of the shape of the combinatorial background on the beam energy is less pronounced than in the case of Λ ($\bar{\Lambda}$).

The invariant mass spectra were fitted to the sum of a polynomial and a signal distribution, determined from the simulation procedure described below. The raw yields of Λ, $\bar{\Lambda}$, Ξ^-, and $\bar{\Xi}^+$ are obtained by subtracting the fitted background and integrating the remaining signal distributions in a mass window of ± 11 MeV/c^2 (± 10 MeV/c^2) around the nominal Λ (Ξ) mass.

C. Correction for acceptance and reconstruction inefficiency

Detailed simulations were made to correct the yields for geometrical acceptance and losses in the reconstruction. For this purpose, samples of Λ and Ξ were generated in the full phase space accessible to the experiment with m_t spectra according to:

$$\frac{1}{m_t}\frac{dN}{dm_t dy} \propto \exp\left(-\frac{m_t}{T}\right). \quad (1)$$

and Gaussian shaped distributions in rapidity y. The Geant 3.21 package [28] was used to track the generated particles and their decay products through the NA49 detector. Dedicated NA49 software was used to simulate the TPC response taking into account all known detector effects. The simulated signals were added to those of real events on the raw data level and subjected to the same reconstruction procedure as the experimental data. The acceptances and efficiencies were calculated in bins of p_t ($m_t - m_0$) and y as the fraction of the generated Λ (Ξ) which traverse the detector, survive the reconstruction and pass the analysis cuts. Of all produced hyperons $\approx 50\%$ (40%) of the Λ (Ξ) appear in the acceptance of the detector, i.e. all decay particles are seen in the sensitive detector volume. The reconstruction algorithm together with the cuts to suppress the combinatorial background reduce this fraction further to $\approx 6\%$ (4%) at 158A GeV. In addition, inefficiencies due to the high track multiplicity cause a further reduction. At 158A GeV this effect is most pronounced and reduces the integrated efficiency to $\approx 2\%$ (1%) for Λ (Ξ). At lower energies the influence of the occupancy is weaker and thus the total efficiency increases to $\approx 4\%$ (2%) at 20A GeV. The upper row of Fig. 2 shows the total reconstruction efficiency which includes acceptance and all reconstruction inefficiencies for Λ and $\bar{\Lambda}$ at the highest beam energy, where the effects of the high track density are largest. Also included in Fig. 2 are efficiencies that have been calculated for two analysis strategies different from the default version described above. The first one (CUT-A, shown as dashed lines) employs a set of selection criteria that depend on the sub-detector in which a V^0 was measured and which were optimized for a large signal-to-background ratio [23]. The second strategy (CUT-B, shown as dotted lines) uses the same cuts as described above, but in addition only accepts tracks which lie outside the high track density region (i.e. 4 cm above or below the middle plane of the TPCs). This criterion allows to minimize the losses due to the high occupancy at the expense of a much reduced acceptance in particular at low p_t. It was used in a previous analysis of the Λ ($\bar{\Lambda}$) at 158A GeV published in [10]. Both approaches drastically reduce the number of reconstructed Λ (Ξ). Therefore, they were not used as the standard procedure in this analysis, but can serve as a cross check that helps to estimate systematic errors (see section II E).

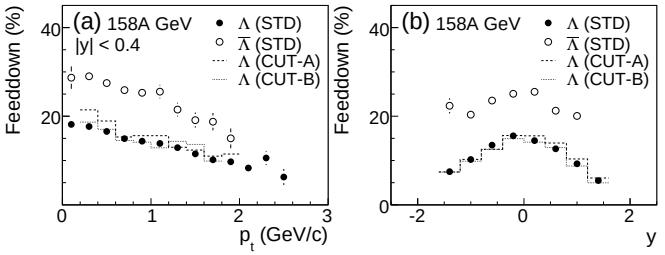

FIG. 3: The feed-down contribution to Λ ($\bar{\Lambda}$) around mid-rapidity as a function of p_t (left panel), and as a function of rapidity (right panel) for central Pb+Pb at 158A GeV. The symbols denote the feed-down for the standard analysis procedure (STD). In addition, the feed-down to Λ for two other selection criteria are shown (dashed: CUT-A, dotted: CUT-B, see text).

D. Correction of feed-down to Λ ($\bar{\Lambda}$)

The measured yield of Λ and $\bar{\Lambda}$ contains, in addition to the directly produced particles, contributions from the decay of heavier hyperons. The Λ ($\bar{\Lambda}$) resulting from electromagnetic decays of Σ^0 ($\bar{\Sigma}^0$) cannot be separated from the directly produced ones. Thus the here presented yields always represent the sum $\Lambda+\Sigma^0$ ($\bar{\Lambda}+\bar{\Sigma}^0$). The contribution to Λ ($\bar{\Lambda}$) from weak decays, however, depends on the chosen analysis cuts, since these decay products originate from decay vertices with a sizable distance from

TABLE II: Summary of the systematic errors on the $\mathrm{d}N/\mathrm{d}y$ values.

	Background subtraction	Efficiency correction	p_t Extra-polation	Feed-down correction	Quadratic sum
Λ	3%	10%	—	1%	10.5%
$\bar{\Lambda}$	3%	10%	—	7%	12.5%
Ξ^-	3%	10%	3%	—	11%
$\bar{\Xi}^+$	3%	10%	3%	—	11%

the main interaction point. Since the NA49 acceptance for Λ ($\bar{\Lambda}$) favours those that decay at large distances, the contribution of feed down Λ ($\bar{\Lambda}$) can be quite substantial. Therefore, we have calculated a correction for the feed-down from $\Xi^- + \Xi^0$ ($\bar{\Xi}^+ + \bar{\Xi}^0$) decays to the measured Λ ($\bar{\Lambda}$) sample with the same simulation procedure as described above for the efficiency correction. In this case a sample of Ξ^- and Ξ^0 ($\bar{\Xi}^+$ and $\bar{\Xi}^0$) was generated as input to the NA49 simulation chain. The feed-down correction was then calculated in bins of p_t ($m_\mathrm{t} - m_0$) and y as the fraction of reconstructed Λ ($\bar{\Lambda}$) which originate from $\Xi^- + \Xi^0$ ($\bar{\Xi}^+ + \bar{\Xi}^0$) decays and pass the same analysis cuts. The input distributions and yields of the Ξ^- ($\bar{\Xi}^+$) are the ones measured by NA49 and presented in this publication. For the Ξ^0 ($\bar{\Xi}^0$), which are not measured, the same phase space distributions were assumed. Their yields are calculated from the ones of Ξ^- ($\bar{\Xi}^+$) which are scaled by the Ξ^0/Ξ^- ($\bar{\Xi}^0/\bar{\Xi}^+$) ratios taken from a statistical model fit [29]. Figure 3 shows as an example the calculated feed-down contribution to Λ ($\bar{\Lambda}$) as a function of p_t and rapidity. The feed-down is largest at low p_t and mid-rapidity and larger for $\bar{\Lambda}$ (20 – 30 % at 158A GeV) than for Λ (5 – 15 % at 158A GeV). While for $\bar{\Lambda}$ no significant dependence of the feed-down on the beam energy is observed, the feed-down to Λ reduces to 3 – 8 % at 20A GeV. Also included in Fig. 3 are the feed-down contributions to Λ for the two alternative analysis strategies described in the previous section (dashed line: CUT-A, dotted line: CUT-B). Since the fraction of Ξ seen in the reconstructed Λ sample depends on the selected analysis cuts, the feed-down contribution has to be evaluated for each approach separately.

E. Systematic errors

There are several contributions to the systematic error which are summarized in Table II. One of them results from uncertainties in the determination of the combinatorial background. This uncertainty can be estimated by varying the degree of the polynomial used to fit the background and the invariant mass range in which the fit is performed. It is found that this systematic error is 3% for Λ and Ξ.

Another contribution arises from imperfections in the description of the detector response by the simulation

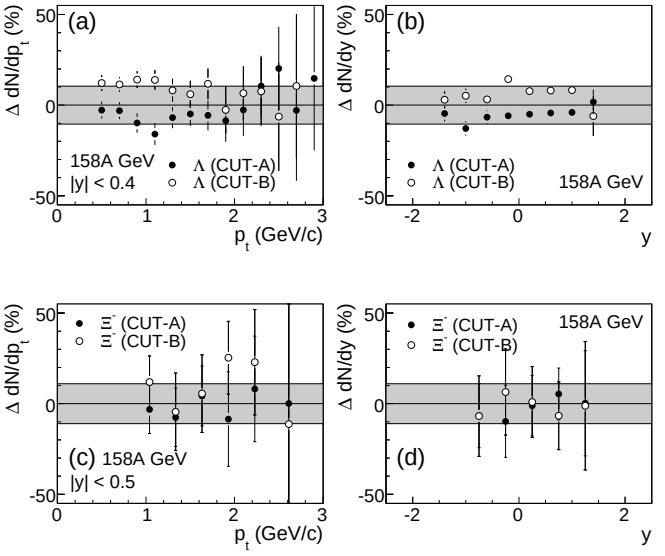

FIG. 4: The differences between the fully corrected results of the standard procedure and of the two alternative analysis strategies (see section II E) for Λ (upper row) and Ξ^- (lower row) in central Pb+Pb at 158A GeV. Shown are the p_t dependence at mid-rapidity (left panels) and the rapidity dependence (right panels). The gray boxes illustrate the systematic error estimate.

procedure which result in systematic uncertainties in the efficiency calculation. It was verified that all distributions of geometrical and kinematical parameters that are relevant in the reconstruction procedure (see section II B) are in agreement between simulated and measured data [30, 31, 32]. Still there can be remaining discrepancies which constitute a source of systematic error. Its magnitude can be estimated by varying the selection criteria in the analysis procedure and checking the consistency of the final result. This was done, e.g., by comparing data points obtained with the alternative analysis strategies described in section II C (CUT-A and CUT-B) to the results for the standard analysis (see Fig. 4). Shown are the differences $\Delta N = N(\mathrm{STD}) - N(\mathrm{CUT\text{-}A(B)})$ as a function of p_t and rapidity, both for Λ and Ξ^-. Even though the efficiencies are lower by almost a factor 2 in some regions of phase space (see Fig. 2) and are subject to different systematic effects (e.g. influence of high track density or background) the results are in agreement. The deviations are consistent with a systematic error of $\approx 10\%$ for Λ and Ξ^- at all beam energies (see Fig. 4). Additionally to the studies presented in Fig. 4, a further investigation was performed in order to test whether the Λ reconstruction is sensitive to the cut applied to the DCA. For this purpose the DCA-cut was relaxed to 1.5 cm (default: 0.5 cm) and the result of this analysis was compared to the standard procedure. It was found that the deviations between the two approaches also agree with the systematic error estimate given in Table II.

TABLE III: The rapidity densities $\mathrm{d}N/\mathrm{d}y$ at mid-rapidity ($\Lambda/\bar{\Lambda}$: $|y| < 0.4$, $\Xi^-/\bar{\Xi}^+$: $|y| < 0.5$), the total multiplicities $\langle N \rangle$, the RMS-widths of the rapidity distributions RMS_{y} calculated from the fits shown in Fig. 9, the averaged transverse masses $\langle m_{\mathrm{t}} \rangle - m_0$, and the inverse slope parameters T at the different beam energies E_{beam}. The first error is statistical, the second systematic.

	E_{beam} (A GeV)	Cent. (%)	$\mathrm{d}N/\mathrm{d}y$	$\langle N \rangle$	RMS_{y}	$\langle m_{\mathrm{t}} \rangle - m_0$ (MeV/c^2)	T (MeV)
Λ	20	7	13.4±0.1±1.1	27.1±0.2±2.2	0.70±0.01±0.06	297± 4±24	244± 3±12
	30	7	14.7±0.2±1.2	36.9±0.3±3.3	0.89±0.02±0.08	310± 5±25	249± 2±13
	40	7	14.6±0.2±1.2	43.1±0.4±4.3	1.11±0.08±0.11	327± 5±27	258± 3±13
	80	7	12.9±0.2±1.0	50.1±0.6±5.5	1.28±0.02±0.14	338± 7±27	265± 4±13
	158	10	9.5±0.1±1.0	44.9±0.6±8.0	—	368± 7±28	301± 4±15
$\bar{\Lambda}$	20	7	0.10±0.02±0.01	0.16±0.02±0.03	0.62±0.14±0.14	407±72±47	339±56±31
	30	7	0.21±0.02±0.02	0.39±0.02±0.04	0.69±0.05±0.08	357±32±30	284±13±26
	40	7	0.33±0.02±0.03	0.68±0.03±0.07	0.77±0.05±0.08	371±22±31	301±10±27
	80	7	0.82±0.03±0.08	1.82±0.06±0.19	0.83±0.05±0.09	363±19±30	292±10±27
	158	10	1.24±0.03±0.13	3.07±0.06±0.31	1.00±0.03±0.09	388±13±31	303± 6±27
Ξ^-	20	7	0.93±0.13±0.10	1.50±0.13±0.17	0.64±0.08±0.07	289±27±29	221±14±13
	30	7	1.17±0.13±0.13	2.42±0.19±0.29	0.73±0.14±0.09	278±19±28	233±11±14
	40	7	1.15±0.11±0.13	2.96±0.20±0.36	0.94±0.13±0.11	285±17±29	222± 9±13
	80	7	1.22±0.14±0.13	3.80±0.26±0.61	0.98±0.25±0.16	317±22±32	227±14±14
	158	10	1.44±0.10±0.15	4.04±0.16±0.57	1.18±0.18±0.17	327±13±33	277± 9±17
$\bar{\Xi}^+$	20	7	—	—	—	—	—
	30	7	0.05±0.01±0.01	0.12±0.02±0.03	0.76±0.35±0.17	326±60±33	311±75±31
	40	7	0.07±0.01±0.01	0.13±0.01±0.02	0.65±0.13±0.09	337±36±34	277±32±28
	80	7	0.21±0.03±0.02	0.58±0.06±0.13	0.87±0.29±0.20	298±38±30	255±23±26
	158	10	0.31±0.03±0.03	0.66±0.04±0.08	0.73±0.08±0.09	384±26±38	321±15±32

In case of Λ and $\bar{\Lambda}$ also the uncertainties in the feed-down contribution have to be taken into account. Here, the errors of the measurements of spectra and yields of Ξ^- and $\bar{\Xi}^+$ translate into a systematic error caused by the feed-down correction. For Λ this error is small (1%), since the correction itself is not too substantial and the Ξ^- measurement is relatively accurate. In case of $\bar{\Lambda}$, however, the larger feed-down contribution and the larger errors of the $\bar{\Xi}^+$ data also result in a larger systematic error of 7%.

In the range of the errors the data presented here agree well with the previously published results where available [10, 23]. The differences compared to the Λ and $\bar{\Lambda}$ yields given in [10] are due to the feed-down contribution which has not been subtracted from the old results.

Since for the Λ ($\bar{\Lambda}$) the range down to $p_{\mathrm{t}} = 0$ GeV/c is measured in most of the rapidity bins, the systematic effects due to extrapolations into unmeasured p_{t} regions is negligible. Only in those y bins where extrapolations are necessary an additional systematic error of 4% is added in quadrature. However, for the Ξ^- ($\bar{\Xi}^+$) analysis, this is introducing an additional systematic error in the full range of the rapidity distributions. It was estimated by using different assumptions for the spectral shape. The standard approach (fit to an exponential, see section IV) was compared to a fit with a hydrodynamically inspired blast wave model [33]. The difference on the $\mathrm{d}N/\mathrm{d}y$ was found to be 3%.

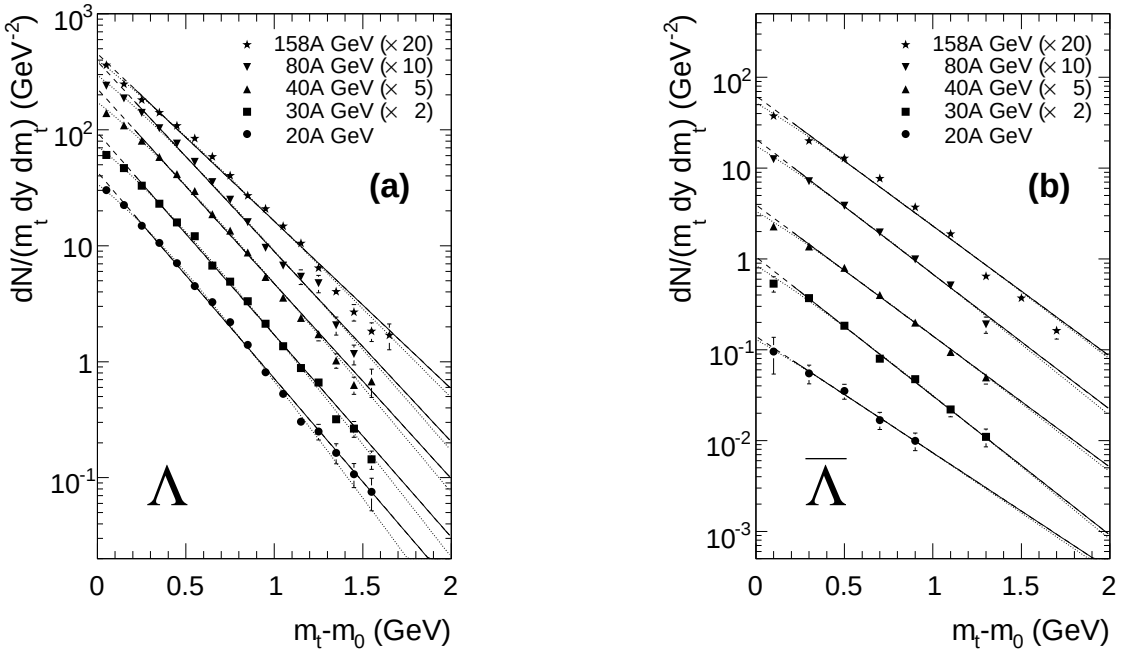

FIG. 5: The transverse mass spectra of Λ (left panel) and $\bar{\Lambda}$ (right panel) at mid-rapidity ($|y| < 0.4$) for 5 different beam energies. The data points are scaled for clarity. Only statistical errors are shown. The solid/dashed lines represent a fit with an exponential, where the solid part denotes the $m_{\rm t}$ range in which the fit was performed. The dotted lines are the results of a fit with a blast wave model [33] (see text for details).

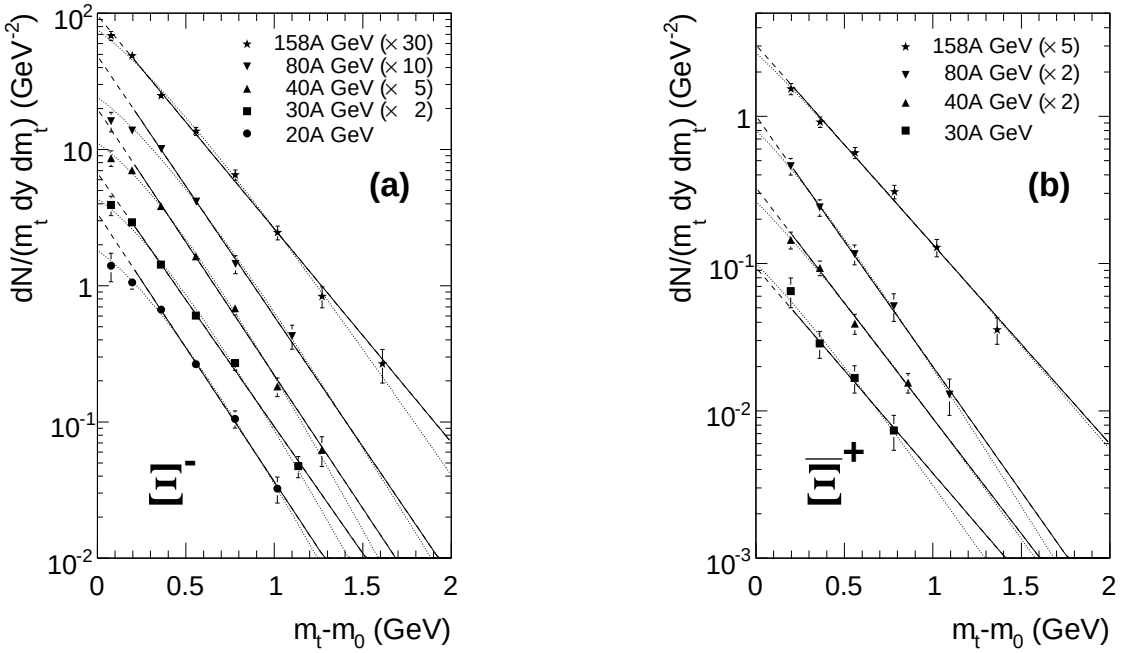

FIG. 6: The transverse mass spectra of Ξ^- (left panel) and $\bar{\Xi}^+$ (right panel) at mid-rapidity ($|y| < 0.5$) for 5 (4) different beam energies. The data points are scaled for clarity. Only statistical errors are shown. The solid/dashed lines represent a fit with an exponential, where the solid part denotes the $m_{\rm t}$ range in which the fit was performed. The dotted lines are the results of a fit with a blast wave model [33] (see text for details).

The extraction of the total multiplicities requires in addition an extrapolation into the unmeasured rapidity regions. The systematic error that is introduced by this extrapolation depends on the beam energy, since the fractions of the longitudinal phase space covered by the measurements also change with energy. Also, the shape of the y spectra is not always very well determined, especially for Λ at 80A and 158A GeV. By using different assumptions for the spectral shape in the unmeasured region, as defined in Eq. (1) and Eq. (2), the additional systematic error on the total multiplicities was estimated. For Λ a variation between 1% at 20A GeV and 14% at 158A GeV was obtained and for $\bar{\Lambda}$ this systematic error is largest at the lowest energy (20%) and decreases to 2% at 158A GeV. In case of the Ξ^- this contribution ranges between 2% at 20A GeV and 12% at 80A GeV, while for the $\bar{\Xi}^+$ it is between 5% (158A GeV) and 20% (30A and 80A GeV).

III. TRANSVERSE MASS SPECTRA

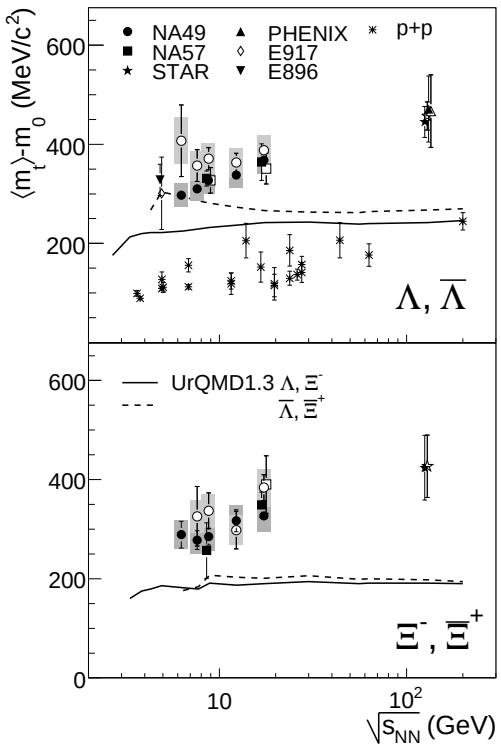

FIG. 7: The $\langle m_t \rangle - m_0$ values for central Pb+Pb and Au+Au reactions as a function of $\sqrt{s_{NN}}$. The systematic errors are represented by the gray boxes. Filled symbols correspond to Λ and Ξ^-, while open symbols denote $\bar{\Lambda}$ and $\bar{\Xi}^+$. Also shown are data from the NA57 collaboration [6, 34], from AGS [35, 36] and RHIC experiments [37, 38, 39], as well as p+p data on Λ [40]. The lines are calculations with the UrQMD1.3 model [41, 42].

The transverse mass spectra of Λ and $\bar{\Lambda}$ measured around mid-rapidity ($|y| < 0.4$) are shown in Fig. 5 and the ones of Ξ^- and $\bar{\Xi}^+$ ($|y| < 0.5$) in Fig. 6. The m_t spectra were fitted by an exponential in the transverse mass range $m_t - m_0 > 0.2$ GeV/c^2 as defined in Eq. (1). The resulting inverse slope parameters T are summarized in Table III. Due to the significant curvature of the m_t spectra equation Eq. (1) does not provide a satisfactory description of the data over the whole m_t range. Therefore, the m_t spectra were additionally fitted by a blast wave model which assumes a transversely expanding emission source [33]. The parameters of this model are the freeze-out temperature T_f and the transverse flow velocity β_s at the surface. Assuming a linear radial velocity profile $\beta_t(r) = \beta_s\, r/R$, which is motivated by hydrodynamical calculations, the m_t spectrum can be computed from

$$\frac{1}{m_t}\frac{dN}{dm_t dy} \propto \int_0^R r\, dr\; m_t\, I_0\left(\frac{p_t \sinh\rho}{T_f}\right) K_1\left(\frac{m_t \cosh\rho}{T_f}\right), \quad (2)$$

where R is the radius of the source and $\rho = \tanh^{-1}\beta_t$ is the boost angle. Since the measurements for the different particle species do not provide an equally good constraint on the fit procedure if both parameters are allowed to vary freely, the transverse flow velocity was fixed to $\langle\beta_t\rangle = 2/3\,\beta_s = 0.4$. The results of the fits are shown as dotted lines in Figs. 5 and 6 and the obtained fit parameters T_f are listed in Table IV. They turn out to be significantly lower for Ξ^- than for Λ at all beam energies. This difference is also visible for the anti-particles, although less pronounced. Even though this observation is based on a relatively simple model, it might indicate that the transverse mass spectra of Λ and Ξ are not determined by the same kinetic freeze-out condition.

TABLE IV: The parameter T_f resulting from the fit with the blast wave model. $\langle\beta_t\rangle$ was fixed in all cases to 0.4. T_f is given in MeV. Errors are statistical only.

Beam energy	$T_f(\Lambda)$	$T_f(\bar{\Lambda})$	$T_f(\Xi^-)$	$T_f(\bar{\Xi}^+)$
20A GeV	100±2	166±38	82±7	—
30A GeV	107±1	134±9	83±5	122±30
40A GeV	115±2	143±7	82±4	127±17
80A GeV	121±2	136±6	95±8	108±12
158A GeV	140±2	146±3	109±5	156±9

To allow for a model independent study of the energy dependence of m_t spectra, the averaged transverse mass $\langle m_t\rangle - m_0$ was calculated. Since for Λ, $\bar{\Lambda}$, and Ξ^- essentially the whole range down to $m_t - m_0 = 0$ is covered, $\langle m_t\rangle - m_0$ can be extracted from the data alone. However, in order to extrapolate up to a common upper limit in $m_t - m_0$, fit functions were used as well. For this purpose two different fits were used: The blast wave model, as shown in Fig. 5, and a fit with a double exponential (not shown) that also provides a good description of the data. The different approaches allow to estimate the systematic error. For $\bar{\Xi}^+$ also an extrapolation to

$m_{\rm t} - m_0 = 0$ is needed.

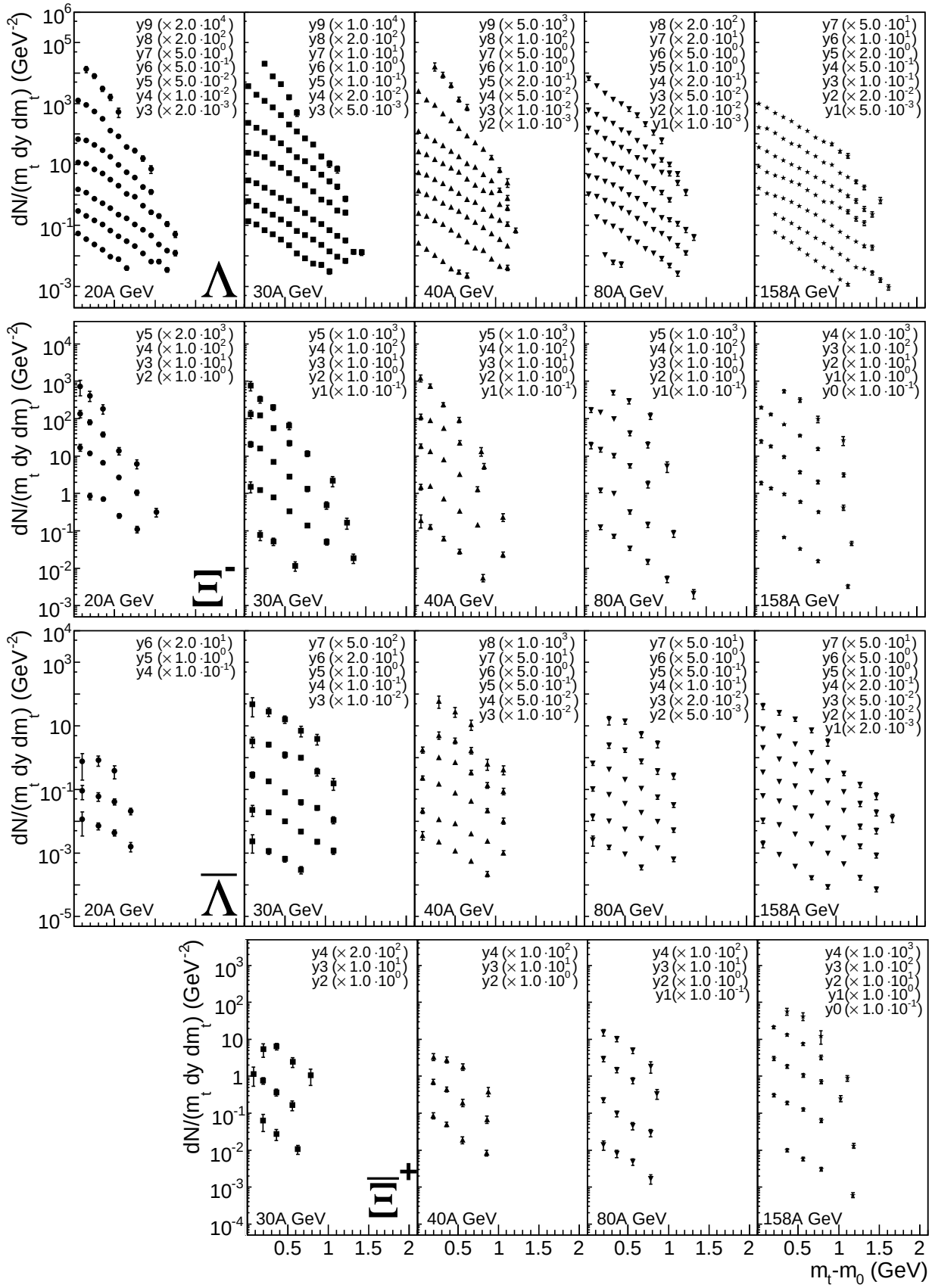

FIG. 8: The transverse mass spectra of Λ, Ξ^-, $\bar{\Lambda}$, and $\bar{\Xi}^+$ for central Pb+Pb collisions in different rapidity bins at 20A, 30A, 40A, 80A, and 158A GeV. Every rapidity bin has a width of 0.4. Bin $y0$ starts at -2.0. The data points are scaled for clarity. Only statistical errors are shown.

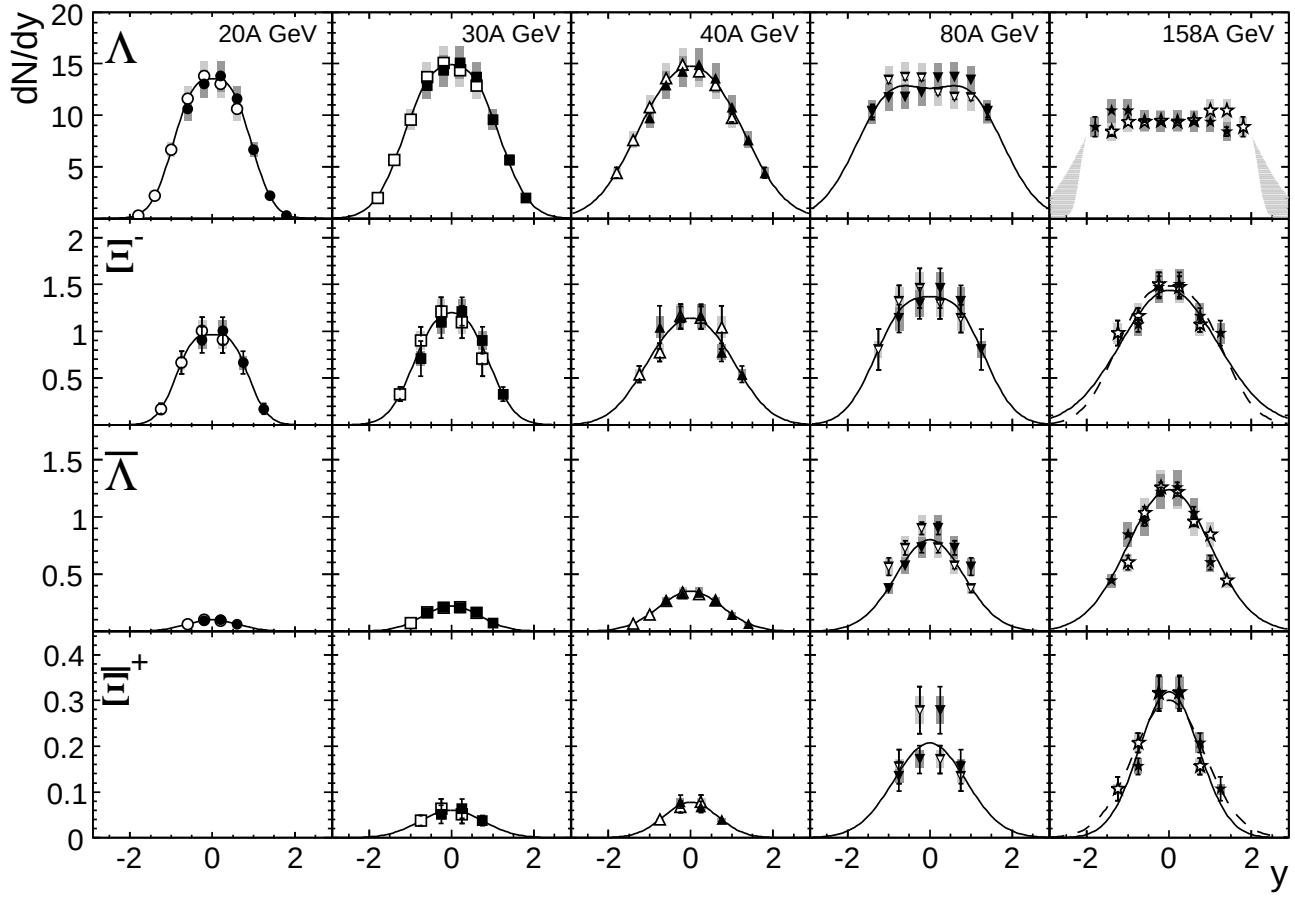

FIG. 9: The rapidity spectra of Λ, Ξ^-, $\bar{\Lambda}$, and $\bar{\Xi}^+$ for 5 different beam energies. The open symbols show data points reflected around mid-rapidity. The systematic errors are represented by the gray boxes. Solid lines are fits to the data points, used to extract the total yields, while dashed lines are the fits to Ξ^- and $\bar{\Xi}^+$ from [23]. The gray area in the Λ spectrum at 158A GeV depicts the uncertainty due to the different extrapolations (see text).

The resulting values for $\langle m_t \rangle - m_0$, corresponding to an interval $0 \leq m_t - m_0 \leq 2$ GeV/c^2, are listed in Table III.

Figure 7 shows the dependence of $\langle m_t \rangle - m_0$ on $\sqrt{s_{NN}}$ for the data presented here in comparison to measurements done by NA57 at the SPS [6, 34], by E896 and E917 at the AGS [35, 36] and by STAR and PHENIX at RHIC [37, 38, 39]. The $\langle m_t \rangle - m_0$ values derived from the NA57 spectra agree with the NA49 results. In the SPS energy range only very little variation of $\langle m_t \rangle - m_0$ with $\sqrt{s_{NN}}$ is observed, followed by a slight increase towards RHIC energies. The $\langle m_t \rangle - m_0$ of Λ is generally higher by ≈ 200 MeV/c^2 than the one observed in p+p reactions [40] at all center-of-mass energies. For pions, kaons and protons a sudden change in the energy dependence of $\langle m_t \rangle - m_0$ around $\sqrt{s_{NN}} = 7 - 8$ GeV was observed [20]. Since currently no data at lower energies are available, it cannot be established whether a similar feature is present in the energy dependence of $\langle m_t \rangle - m_0$ for hyperons. However, the remarkably small energy variation shown in Fig. 7 would still be in line with the behavior observed for the other particle species.

TABLE V: The parameter σ and y_0 resulting from the fits with the sum of two Gauss functions (see Eq. (3)) to the rapidity distributions of Λ and Ξ^-.

Beam energy	$\sigma(\Lambda)$	$y_0(\Lambda)$	$\sigma(\Xi^-)$	$y_0(\Xi^-)$
20A GeV	0.51±0.01	0.49±0.01	0.45±0.08	0.45±0.07
30A GeV	0.66±0.02	0.59±0.01	0.56±0.15	0.47±0.11
40A GeV	0.91±0.06	0.65±0.04	0.76±0.16	0.54±0.12
80A GeV	0.87±0.07	0.94±0.06	0.71±0.32	0.68±0.13
158A GeV	—	—	1.18±0.18	—

The measurements on $\langle m_t \rangle - m_0$ are also compared to the string hadronic model UrQMD1.3. While this model in principle reproduces the observed near independence of $\langle m_t \rangle - m_0$ on $\sqrt{s_{NN}}$ in the SPS energy region, it fails to match its magnitude. The calculation is always ≈ 100 MeV below the data. Additionally, this version of UrQMD does not describe the slow increase towards RHIC.

IV. RAPIDITY SPECTRA

Figure 8 summarizes the m_t spectra of Λ, Ξ^-, $\bar{\Lambda}$, and $\bar{\Xi}^+$ as measured in different rapidity bins. The data points cover a large fraction of the phase space and thus allow to extract rapidity distributions by integrating the transverse mass spectra. Table III summarizes the resulting rapidity densities around mid-rapidity and Fig. 9 shows the resulting y spectra. For Λ a clear evolution of the spectral shape with beam energy is observed. While the rapidity spectrum at 20A GeV has an almost Gaussian shape, a plateau around mid-rapidity is developing that widens with increasing energy. At 158A GeV the spectrum is finally constant in the measured rapidity range. This reflects the continuous change of the rapidity distribution of the net-baryon number in this energy range [43]. While at lower energies the final state distribution of the incoming nucleons looks thermal, the rapidity distribution of the net-baryons develops a distinct minimum at mid-rapidity with increasing energy due to incomplete stopping. Since Λ carry a significant fraction of the net-baryon number they follow this change to a large extent. A similar behavior, although less pronounced, is visible for the Ξ^- as well. $\bar{\Lambda}$ and $\bar{\Xi}^+$, on the other hand, are well described by Gaussians at all beam energies.

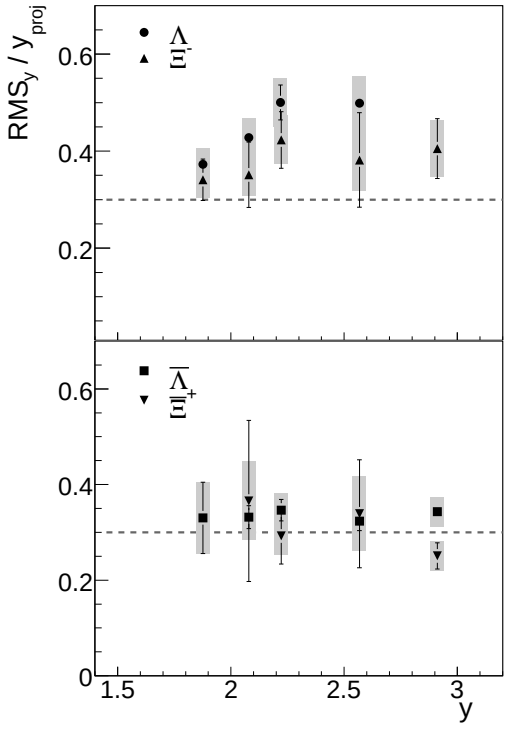

FIG. 10: The RMS widths of the rapidity distributions RMS_y, normalized by the projectile rapidity y_{proj}, as a function of y_{proj}. The systematic errors are represented by the gray boxes.

In order to determine total multiplicities, extrapolations into the unmeasured y regions are needed. Therefore, Λ and Ξ^- were fitted with a sum of two Gauss functions placed symmetrically around mid-rapidity

$$\frac{dN}{dy} \propto \exp\left\{-\frac{(y-y_0)^2}{2\sigma^2}\right\} + \exp\left\{-\frac{(y+y_0)^2}{2\sigma^2}\right\}. \quad (3)$$

The resulting fit parameters are listed in Table V. In case of the Ξ^- at 158A GeV a single Gaussian turned out to provide a better fit to the data (solid line in Fig. 9). For the Λ distribution at 158A GeV a fit cannot be performed since the measurement does not allow to determine the end of the dN/dy distribution. Here, the extrapolation has to be based on different assumptions on the spectral shape. An upper limit on the contribution from the

unmeasured parts can be derived by using the measured net-proton distribution at 158A GeV [44] to describe the tails. Another approach is to assume the same shape for the Λ rapidity distribution as has been measured for central S+S reactions at 200A GeV [4], which then results in a lower total yield. The multiplicity quoted in Table III is the average between both extrapolations and their difference is taken as its systematic error.

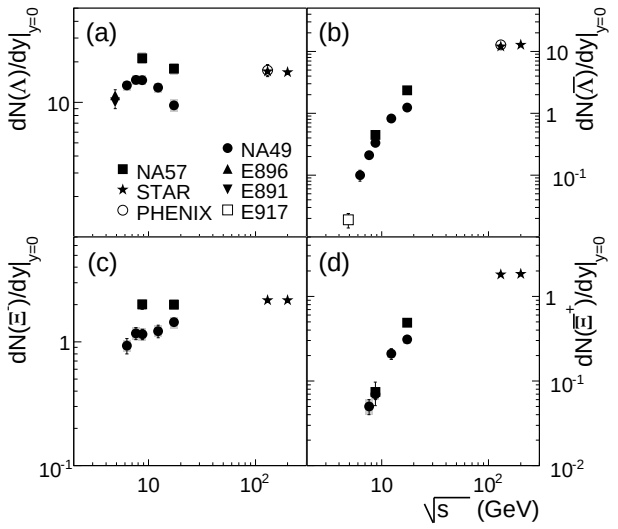

FIG. 11: The rapidity densities dN/dy at mid-rapidity ($\Lambda/\bar{\Lambda}$: $|y| < 0.4$, $\Xi^-/\bar{\Xi}^+$: $|y| < 0.5$) in central Pb+Pb and Au+Au collisions as a function of $\sqrt{s_{\rm NN}}$. The systematic errors are represented by gray areas, mostly hidden by the symbols. Also shown are data from the NA57 collaboration [6, 34], as well as from AGS [35, 36, 45] and RHIC experiments [37, 38, 39, 46].

For $\bar{\Lambda}$ and $\bar{\Xi}^+$ a single Gauss function was used to derive the total yields. The resulting fit parameters σ are identical to the values for $RMS_{\rm y}$ tabulated in Table III. The rapidity spectra of Ξ^- and $\bar{\Xi}^+$ at 158A GeV also agree well with a fit to the previously published data (dashed lines in Fig. 9). Figure 10 summarizes the energy dependence of the $RMS_{\rm y}$ values. While the widths of the $\bar{\Lambda}$ and $\bar{\Xi}^+$ distributions agree with each other and exhibit an approximately linear dependence on the projectile rapidity $y_{\rm proj}$ ($RMS_{\rm y} \approx 0.3\, y_{\rm proj}$, see dashed line in Fig. 10), the Λ and Ξ^- show a different behavior. Here $RMS_{\rm y}/y_{\rm proj}$ is larger and also clearly energy dependent. The effect is more pronounced for the Λ than for the Ξ^-.

V. PARTICLE YIELDS

Figure 11 shows the rapidity densities around mid-rapidity as a function of $\sqrt{s_{\rm NN}}$. The energy dependence of dN/dy for Λ exhibits a complicated structure. It rises from AGS to a maximum at a beam energy of 30A GeV, then drops towards top SPS energy and rises again slowly to $\sqrt{s_{\rm NN}} = 130$ GeV. This can be understood by an interplay of the slow rise of the Λ multiplicity from $E_{\rm beam} = 30A$ GeV on (see Fig. 13a) and the pronounced change of shape seen in the rapidity distribution in the same energy region (see Fig. 9). Since the Λ yield gets distributed more and more evenly along the rapidity axis, the mid-rapidity dN/dy is reduced above $E_{\rm beam} = 30A$ GeV. At some point the redistribution along y is compensated again by the further increase of the Λ multiplicity, so that the rapidity density dN/dy is again higher at RHIC. Such a significant structure in the energy dependence is not observed for the Ξ^-, where the mid-rapidity dN/dy increases more smoothly by a factor of ≈ 2 from $E_{\rm beam} = 20A$ GeV towards RHIC. However, also here a small structure in the energy dependence is visible between 20A and 80A GeV. For $\bar{\Lambda}$ and $\bar{\Xi}^+$, where no change in the shape of the dN/dy spectra is seen, the mid-rapidity dN/dy values increase rapidly over $\approx$2 orders of magnitude between $E_{\rm beam} = 20A$ GeV and $\sqrt{s_{\rm NN}} = 130$ GeV.

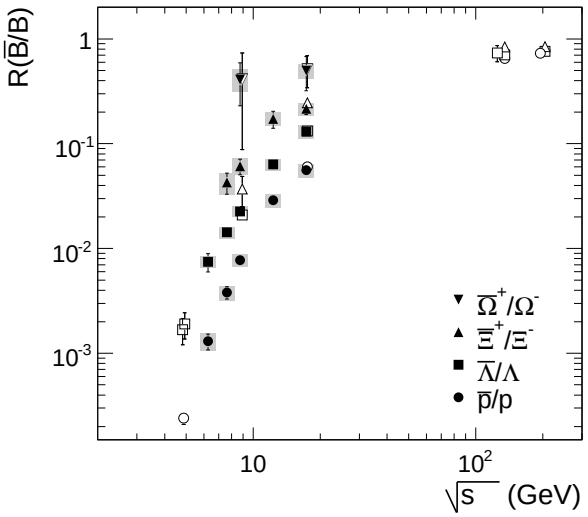

FIG. 12: The $\bar{\rm p}$/p [47], $\bar{\Lambda}/\Lambda$, $\bar{\Xi}^+/\Xi^-$, and $\bar{\Omega}^+/\Omega^-$ [11] ratios around mid-rapidity (Λ: $|y| < 0.4$, Ξ and Ω: $|y| < 0.5$) in central Pb+Pb and Au+Au collisions as a function of $\sqrt{s_{\rm NN}}$. Also shown as open symbols are data from the SPS experiments NA44 [48] and NA57 [6, 34], from AGS [35, 36, 45, 49] and RHIC experiments [37, 38, 39, 46, 50, 51, 52]. The symbols are slightly displaced for clarity.

It should be noted that at this point there is a significant disagreement between the measurements presented here and the data published by the NA57 collaboration [6, 34]. Even though the NA57 data follow the same trend in the energy dependence, they are systematically higher than the NA49 results [64]. This discrepancy is generally of the order of 1 – 2.5 standard deviations with the only exception of the $\bar{\Xi}^+$ measurements at 40A GeV. The measured particle ratios, on the other hand, show a good agreement between the two experiments. Despite intensive discussions between both collaborations, the origin of the discrepancies is not yet found.

The energy dependence of the antibaryon/baryon ra-

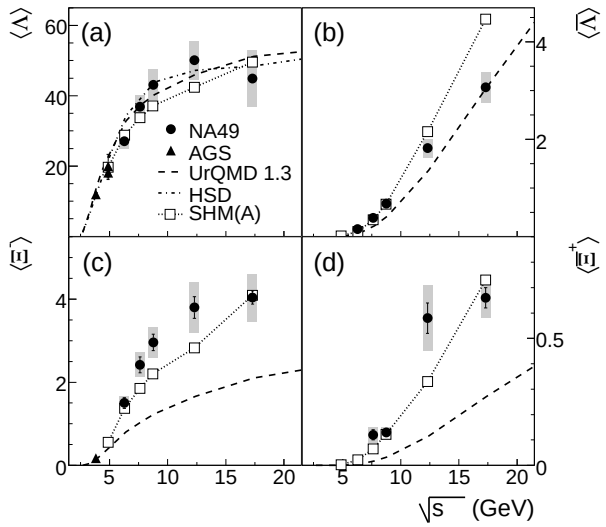

FIG. 13: The total multiplicities of Λ (a), $\bar{\Lambda}$ (b), Ξ^- (c), and $\bar{\Xi}^+$ (d) in central Pb+Pb and Au+Au collisions as a function of $\sqrt{s_{\rm NN}}$. The systematic errors are represented by the gray boxes. Also shown are AGS data [9, 35, 45], as well as calculations with string hadronic models (HSD, UrQMD1.3 [41, 42, 53]) and with a statistical hadron gas model (SHM(A) [29]).

tios $R(\bar{\rm B}/{\rm B})$, measured at mid-rapidity, are compared for protons, Λ, Ξ, and Ω in Fig. 12. The ratios exhibit a rapid rise for all particle species over several orders of magnitude in the SPS energy range and converge towards values close to 1 at RHIC energies. There is a distinct hierarchy of the ratios, depending on the strangeness content of the baryons:

$$R(\bar{\Omega}^+/\Omega^-) > R(\bar{\Xi}^+/\Xi^-) > R(\bar{\Lambda}/\Lambda) > R(\bar{\rm p}/{\rm p}).$$

Also, the energy dependence in the SPS region gets slightly weaker with increasing strangeness. The $\bar{\rm B}/{\rm B}$ ratios at mid-rapidity directly reflect the drastic change in the net-baryon number. However, the sensitivity depends to some extent on the valence quark content of the baryon which is thus responsible for the observed hierarchy.

The total multiplicities, as determined from the ${\rm d}N/{\rm d}y$ spectra shown in Fig. 9, are compiled in Fig. 13 together with AGS data where available [9, 35, 45]. The total multiplicities of Λ and Ξ^- increase quite rapidly at lower energies, while from $\sqrt{s_{\rm NN}} \approx 8$ GeV on they rise only moderately with energy. $\bar{\Lambda}$ and $\bar{\Xi}^+$, on the other hand, exhibit a continuous fast increase with beam energy. The measurements are confronted with several hadronic models. In Fig. 13a calculations with the string hadronic models HSD [53] and UrQMD1.3 [41] for $\langle\Lambda\rangle$ as a function of $\sqrt{s_{\rm NN}}$ are shown, as well as results from a fit with a statistical hadron gas model [29] (SHM(A)). All three models are able to describe the data satisfactorily. A similar picture is observed for $\langle\bar{\Lambda}\rangle$ (see Fig. 13b), although the fit with the statistical hadron gas model seems to overpredict the measurements at $E_{\rm beam} = 80A$ and 158A GeV. The difference between UrQMD1.3 and the statistical model is more pronounced for Ξ^- and $\bar{\Xi}^+$ (see Fig. 13c and d). While the data points at SPS energies are above the UrQMD1.3 calculation by a factor of ≈ 2, the statistical model fit provides a qualitative description of the measurement, although the agreement is not perfect.

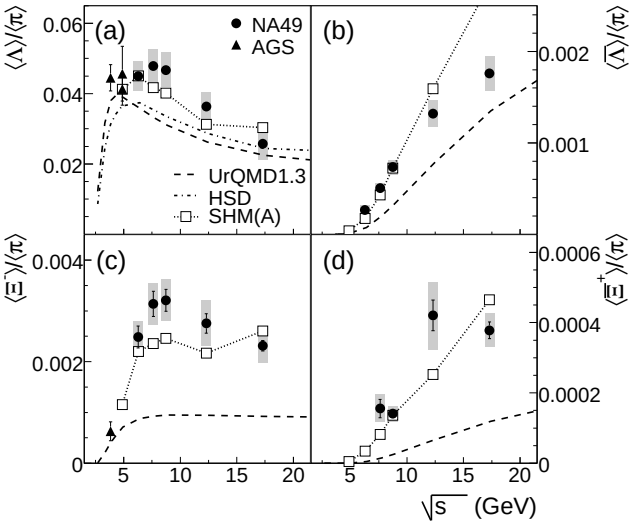

FIG. 14: The total multiplicities of Λ (a), $\bar{\Lambda}$ (b), Ξ^- (c), and $\bar{\Xi}^+$ (d) divided by the total pion multiplicities ($\langle\pi\rangle = 1.5\,(\langle\pi^+\rangle + \langle\pi^-\rangle)$) in central Pb+Pb and Au+Au collisions as a function of $\sqrt{s_{\rm NN}}$. The systematic errors are represented by the gray boxes. Also shown are AGS data [9, 35, 45, 54, 55], as well as calculations with string hadronic models (HSD, UrQMD1.3 [41, 42, 53]) and a statistical hadron gas model (SHM(A) [29]).

In Fig. 14 the total multiplicities of hyperons divided by the total number of pions $\langle\pi\rangle = 1.5\ (\langle\pi^+\rangle + \langle\pi^-\rangle)$ are compiled. The $\langle\Lambda\rangle/\langle\pi\rangle$ and the $\langle\Xi^-\rangle/\langle\pi\rangle$ ratios have distinct maxima in the region $\sqrt{s_{\rm NN}} = 7$ – 9 GeV, while the $\langle\bar{\Lambda}\rangle/\langle\pi\rangle$ and $\langle\bar{\Xi}^+\rangle/\langle\pi\rangle$ ratios increase monotonously with energy. The comparison to the string hadronic model results of HSD and of UrQMD1.3 reveals a significant disagreement with the $\langle\Lambda\rangle/\langle\pi\rangle$ and $\langle\bar{\Lambda}\rangle/\langle\pi\rangle$ ratios (see Fig. 14a and b), which is not present in the Λ and $\bar{\Lambda}$ multiplicities alone as shown in Fig. 13a and b. This is a reflection of the fact that these models overpredict the pion production at top AGS and lower SPS energies [42, 62]. Hence, the disagreement with the $\langle\Xi^-\rangle/\langle\pi\rangle$ and $\langle\bar{\Xi}^+\rangle/\langle\pi\rangle$ ratios (Fig. 14c and d) is even more pronounced than for the Ξ multiplicities alone. The statistical hadron gas model approach provides overall a better description of the measured particle ratios than UrQMD1.3. However, the $\langle\bar{\Lambda}\rangle/\langle\pi\rangle$ ratio is clearly overestimated at higher energies by SHM(A), while the fit results from this model are slightly below the data points for $\langle\Xi^-\rangle/\langle\pi\rangle$ and $\langle\bar{\Xi}^+\rangle/\langle\pi\rangle$ for $\sqrt{s_{\rm NN}} < 17.3$ GeV. In [63] it was argued that a statistical model approach predicts different positions of the maxima in the energy dependence of $\langle\Lambda\rangle/\langle\pi\rangle$ ($\sqrt{s_{\rm NN}}({\rm max}) = 5.1$ GeV) and of

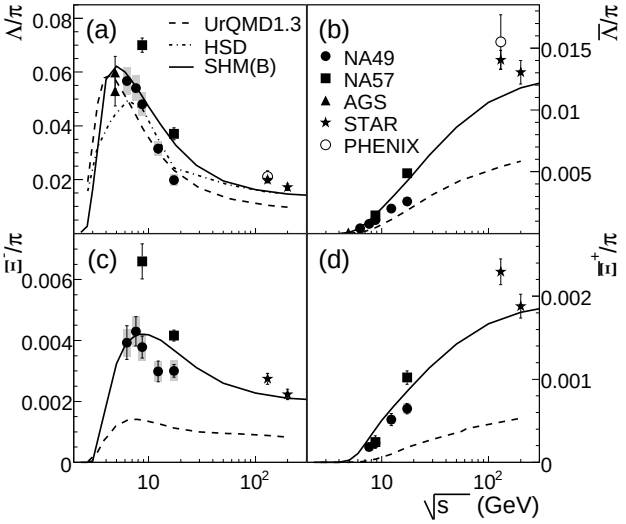

FIG. 15: The rapidity densities $\mathrm{d}N/\mathrm{d}y$ at mid-rapidity of Λ (a), $\bar{\Lambda}$ (b), Ξ^- (c), and $\bar{\Xi}^+$ (d) divided by the pion rapidity densities ($\pi = 1.5\,(\pi^+ + \pi^-)$) in central Pb+Pb and Au+Au collisions as a function of $\sqrt{s_{\mathrm{NN}}}$. The systematic errors are represented by the gray boxes. Also shown are NA57 [6, 34], AGS [35, 36, 45, 55], and RHIC [37, 38, 39, 46, 56, 57, 58] data, as well as calculations with string hadronic models (HSD, UrQMD1.3 [41, 42, 53]) and a statistical hadron gas model (SHM(B) [59]).

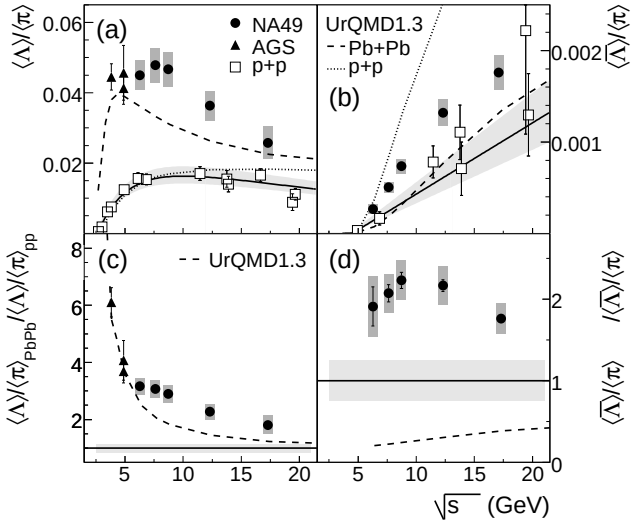

FIG. 16: The total multiplicities of Λ (a) and $\bar{\Lambda}$ (b) divided by the total pion multiplicities ($\langle\pi\rangle = 1.5\,(\langle\pi^+\rangle + \langle\pi^-\rangle)$) for central Pb+Pb and Au+Au collisions as a function of $\sqrt{s_{\mathrm{NN}}}$. The systematic errors are represented by the gray boxes. Also shown are AGS data [9, 35, 45, 54, 55], measurements for p+p collisions by other experiments (open squares) [60, 61], as well as a calulation with the UrQMD1.3 model (dashed line: Pb+Pb, dotted line p+p). The solid line represents a parametrization of the p+p data (see text). The enhancements relative to the p+p parametrization are shown in panels (c) and (d). The gray boxes denote the uncertainty of the p+p reference parametrization. The dashed line represents the values from the UrQMD1.3 model.

$\langle\Xi^-\rangle/\langle\pi^-\rangle$ ($\sqrt{s_{\mathrm{NN}}}(\mathrm{max}) = 10.2$ GeV). However, the existing measurements do not allow to determine the exact positions of the maxima with the required precision in order to establish a significant difference. For this purpose also more data at lower energies ($\sqrt{s_{\mathrm{NN}}} < 6$ GeV) with high precision would be required.

Qualitatively the same picture emerges when the ratios of the mid-rapidity yields are studied instead of the ratios of total yields, as shown in Fig. 15 together with results from RHIC experiments. Again, the string hadronic models HSD and UrQMD1.3 fail to match the Ξ^-/π and $\bar{\Xi}^+/\pi$ ratios, even though a reasonable description of the Λ/π and $\bar{\Lambda}/\pi$ ratios at SPS energies is achieved, and statistical models provide generally a better description. As an alternative implementation of the statistical hadron gas model here the one by [13, 59] (SHM(B)) is used. While in SHM(A) [29] a separate fit at each energy to all available particle multiplicities is performed by varying chemical freeze-out temperature T_{ch} and baryonic chemical potential μ_{B}, the input parameters T_{ch} and μ_{B} in SHM(B) [59] are taken from a smooth parametrization of the $\sqrt{s_{\mathrm{NN}}}$-dependence of the original fit results. In addition, the model SHM(A) includes a parameter to allow for strangeness undersaturation γ_{s}, which is not present in model SHM(B) (i.e. $\gamma_{\mathrm{s}} = 1$). Both models use a grand canonical ensemble for the results shown here. In the case of model SHM(B) an additional correction by a canonical suppression factor is applied. However, for central A+A collisions this correction is only effective at AGS energies ($\sqrt{s_{\mathrm{NN}}} \leq 5$ GeV) [59]. Thus, SHM(B) provides a baseline defining the state of maximal chemical equilibrium that is attainable. However, the parametrization that provides the basis of SHM(B) has been tuned to fit mid-rapidity ratios, while the fits with SHM(A) have been done for total multiplicities which complicates a direct comparison between the two approaches. SHM(B), as shown in Fig. 15, generally overpredicts all measured mid-rapidity ratios at the higher SPS energies ($\sqrt{s_{\mathrm{NN}}} = 12 - 17$ GeV), while at lower SPS and at RHIC energies a satisfactory agreement is achieved. Therefore, in the data a sharper maximum in the energy dependence of the Λ/π and Ξ^-/π ratios is observed than in the model. The NA57 results[65] exibit a similarly shaped energy dependence. However, the ratios are generally higher than the NA49 results.

The observed maxima in the Λ/π and Ξ^-/π ratios occur in the same energy range as the observed distinct peak in the K^+/π^+ ratio [20]. Since the latter can be interpreted as a signature for the onset of deconfinement, the question appears whether the maxima in the Λ/π and Ξ^-/π ratios can be attributed to the same effect. In contrast to the K^+, which carry together with the K^0 the bulk of the anti-strange quarks and are thus a relatively direct measure of the strangeness production, the interpretation of the strange baryons is complicated by the fact that their sensitivity to the strangeness pro-

duction is strongly modified by the energy dependent baryon number distributions. At low energies, with high baryonic chemical potential, the production of baryons is favoured and more strange quarks will end up in Λ and Ξ^-, compared to higher energies where strange quarks might predominantly be contained in K^- and $\bar{K}^0$. This is underlined by the fact that the statistical model approaches, which reflect the dependence of particle yields on μ_B, provide a relatively good describtion of the data. Whether the remaining discrepancies between SHM(B) and the mid-rapidity ratios at 80A and 158A GeV (see Fig. 15, panels (a) and (c)) might be attributed to the onset of deconfinement can in the light of the systematic uncertainties not be definitely answered. However, one should keep in mind that the mid-rapidity Λ/π and Ξ^-/π ratios are also strongly affected by the rapid change of the shape of the Λ and Ξ^- rapidity distributions with energy. This effect will cause a more pronounced energy dependence of the mid-rapidity ratios in comparison to the 4π ratios, which in principle cannot be described by statistical models.

The $\langle\Lambda\rangle/\langle\pi\rangle$ and $\langle\bar{\Lambda}\rangle/\langle\pi\rangle$ ratios, as measured in central nucleus–nucleus collisions, are compared to data obtained in p+p collisions [60, 61] in Fig. 16. The p+p measurements were parametrized by a fit function. For $\langle\Lambda\rangle/\langle\pi\rangle$ the following function with the fit parameters a, b, and c was used:

$$\langle\Lambda\rangle/\langle\pi\rangle(p+p) = c[1-\exp(-(\sqrt{s}-\sqrt{s_0})/a)+b(\sqrt{s}-\sqrt{s_0})] \quad (4)$$

Here, $\sqrt{s_0}$ denotes the threshold center-of-mass energy. The result of the fit is displayed in Fig. 16a. It provides a reasonable description of the available data in the energy range of $\sqrt{s_{NN}} < 20$ GeV. Similarly, the energy dependence of the $\langle\bar{\Lambda}\rangle/\langle\pi\rangle$ ratio was parametrized by a straight line. However, the existing measurements are much less precise than in the $\langle\Lambda\rangle/\langle\pi\rangle$ case. Based on these parametrizations, the energy dependence of an enhancement factor E relative to p+p, defined as

$$E = \langle N\rangle/\langle\pi\rangle|_{A+A} \,/\langle N\rangle/\langle\pi\rangle|_{p+p} \quad (5)$$

can be determined. As shown in Fig. 16c, the enhancement factor for Λ exhibits a clear increase from a factor of $\approx$2 to >3 towards lower energies. For $\sqrt{s_{NN}} < 4$ GeV the AGS measurement of [9] suggests an even more dramatic rise towards very low energies. For $\bar{\Lambda}$ the enhancement is of the order of ≈ 2, without any significant energy dependence in the range covered by the data. While the UrQMD1.3 model qualitatively reproduces the energy dependence of the Λ-enhancement, it fails to describe the enhancement of $\bar{\Lambda}$. In fact, the model rather predicts a $\bar{\Lambda}$-suppression, which is mainly due to the fact that the $\langle\bar{\Lambda}\rangle/\langle\pi\rangle$ ratio in p+p reactions is grossly overestimated (see dotted line in Fig. 16,b). Since the net-baryon density is largest around $\sqrt{s_{NN}} = 5$ GeV, the production of strange baryons exhibits a pronounced maximum at these energies. This effect is described by all hadronic models considered here and consequently the Λ/π-ratios are well reproduced (Figs. 14 and 15). Moreover, the energy dependence of the Λ-enhancement seems to be affected by the redistribution of the baryon number, which is suggested by the fact that UrQMD1.3 gives a similar increase towards low energies. In comparison, the doubly strange Ξ^- is less sensitive to the baryon number density and more to the overall strangeness production, which may explain why string hadronic models fail to describe the data. For the corresponding antiparticles this argument applies even more strongly. Whether the Ξ-enhancement also increases towards low energies, similar to the Λ, can currently not be decided due to the lack of precise reference data in p+p at lower energies.

VI. SUMMARY

A systematic study of the energy dependence of Λ, $\bar{\Lambda}$, Ξ^-, and $\bar{\Xi}^+$ production in central Pb+Pb reactions at SPS energies is presented.

The shape of the m_t spectra exhibits only a weak dependence on beam energy, which is also reflected in the moderate increase of $\langle m_t\rangle - m_0$ towards the higher RHIC energies. A similar behavior was also observed for pions, kaons, and protons. For these particles a sudden change in the energy dependence around $\sqrt{s_{NN}} = 7$ – 8 GeV was found in addition. Due to the lack of data at lower energies it currently cannot be established whether a similar feature is present in the energy dependence of $\langle m_t\rangle - m_0$ for hyperons. There is an indication for a slightly weaker energy dependence of $\langle m_t\rangle - m_0$ for $\bar{\Lambda}$ than for Λ, the values for $\bar{\Lambda}$ being above the ones for Λ. Generally, the measured $\langle m_t\rangle - m_0$ is higher for all investigated particle species than what is predicted by the UrQMD1.3 model.

For Λ and Ξ^- rapidity spectra a clear change of the shape is observed. The almost Gaussian like spectral form develops a plateau around mid-rapidity towards higher energies, reflecting the change of the longitudinal distribution of the net-baryon number. The rapidity spectra of $\bar{\Lambda}$ and $\bar{\Xi}^+$, on the other hand, can be described by single Gaussians at all investigated energies, whose σ increases monotonically with energy.

Also the energy dependence of the total yields shows a distinct difference between baryons and anti-baryons. While for the $\bar{\Lambda}$ and $\bar{\Xi}^+$ multiplicities a continuous rapid rise with beam energy is observed, the increase of the Λ and Ξ^- yields is clearly weaker above $\sqrt{s_{NN}} = 7$ – 8 GeV than below. This difference gets even more pronounced when dividing the total multiplicities of the hyperons by those of pions. The energy dependence of the $\langle\Lambda\rangle/\langle\pi\rangle$ and $\langle\Xi^-\rangle/\langle\pi\rangle$ ratios exhibits significant maxima in the region $5 < \sqrt{s_{NN}} < 10$ GeV, while the $\langle\bar{\Lambda}\rangle/\langle\pi\rangle$ and $\langle\bar{\Xi}^+\rangle/\langle\pi\rangle$ ratios increase monotonically. The total multiplicities of Λ and $\bar{\Lambda}$ are well described by the string hadronic UrQMD1.3 model. However, Ξ^- and $\bar{\Xi}^+$ multiplicities are underpredicted by factors of 2 – 3 at SPS energies. A better overall description of all measured yields is provided by statistical hadron gas models.

Acknowledgments

This work was supported by the US Department of Energy Grant DE-FG03-97ER41020/A000, the Bundesministerium für Bildung und Forschung, Germany (06F137), the Virtual Institute VI-146 of Helmholtz Gemeinschaft, Germany, the Polish State Committee for Scientific Research (1 P03B 006 30, N N202 078735, 1 PO3B 121 29, 1 P03B 127 30), the Hungarian Scientific Research Foundation (T032648, T032293, T043514), the Hungarian National Science Foundation, OTKA, (F034707), the Polish-German Foundation, the Korea Research Foundation (KRF-2007-313-C00175) and the Bulgarian National Science Fund (Ph-09/05).

[1] J. Rafelski and B. Müller, Phys. Rev. Lett. **48**, 1066 (1982).
[2] P. Koch, B. Müller, and J. Rafelski, Phys. Rep. **142**, 167 (1986).
[3] J. Bartke et al. (NA35 Collaboration), Z. Phys. C **48**, 191 (1990).
[4] T. Alber et al. (NA35 Collaboration), Z. Phys. C **64**, 195 (1994).
[5] F. Antinori et al. (WA97 Collaboration), Eur. Phys. J. C **11**, 79 (1999).
[6] F. Antinori et al. (NA57 Collaboration), J. Phys. G **32**, 427 (2006).
[7] M. Mitrovski (for the NA49 Collaboration), J. Phys. G **32**, S43 (2006).
[8] L. Ahle et al (E802 Collaboration), Phys. Rev. C **60**, 044904 (1999).
[9] P. Chung et al. (E895 Collaboration), Phys. Rev. Lett. **91**, 202301 (2003).
[10] T. Anticic et al. (NA49 Collaboration), Phys. Rev. Lett. **93**, 022302 (2004).
[11] C. Alt et al. (NA49 Collaboration), Phys. Rev. Lett. **94**, 192301 (2005).
[12] F. Becattini, J. Cleymans, A. Keranen, E. Suhonen, and K. Redlich, Phys. Rev. C **64**, 024901 (2001).
[13] P. Braun-Munzinger, J. Cleymans, H. Oeschler, and K. Redlich, Nucl. Phys. A **697**, 902 (2002).
[14] C. Greiner and S. Leupold, J. Phys. G **27**, L95 (2001).
[15] P. Braun-Munzinger, J. Stachel, and C. Wetterich, Phys. Lett. B **596**, 61 (2004).
[16] F. Becattini, M. Gaździcki, and J. Sollfrank, Eur. Phys. J. C **5**, 143 (1998).
[17] F. Becattini, M. Gaździcki, A. Keranen, J. Manninen, and R. Stock, Phys. Rev. C **69**, 024905 (2004).
[18] U. Heinz, Nucl. Phys. A **638**, 357c (1998).
[19] R. Stock, Phys. Lett. B **456**, 277 (1999).
[20] C. Alt et al. (NA49 Collaboration), Phys. Rev. C **77**, 024903 (2008).
[21] M. Gaździcki and M. I. Gorenstein, Acta Phys. Polon. B **30**, 2705 (1999).
[22] M. I. Gorenstein, M. Gaździcki, and K. A. Bugaev, Phys. Lett. B **567**, 175 (2003).
[23] S. V. Afanasiev et al. (NA49 Collaboration), Phys. Lett. B **538**, 275 (2002).
[24] A. Richard (for the NA49 Collaboration), J. Phys. G **31**, S155 (2005).
[25] C. Meurer (for the NA49 Collaboration), J. Phys. G **30**, S1325 (2004).
[26] S. V. Afanasiev et al. (NA49 Collaboration), Nucl. Instrum. Meth. A **430**, 210 (1999).
[27] W.-M. Yao et al. (Particle Data Group), J. Phys. G **33**, 1 (2006).
[28] Geant—Detector Description and Simulation Tool, CERN Program Library Long Writeup W5013.
[29] F. Becattini, J. Manninen, and M. Gaździcki, Phys. Rev. C **73**, 044905 (2006).
[30] M. Mitrovski, PhD thesis, University of Frankfurt (2007).
[31] A. Richard, Diploma thesis, University of Frankfurt (2004).
[32] C. Meurer, Diploma thesis, University of Frankfurt (2003).
[33] E. Schnedermann and U. Heinz, Phys. Rev. C **50**, 1675 (1994).
[34] F. Antinori et al. (NA57 Collaboration), Phys. Lett. B **595**, 68 (2004).
[35] S. Albergo et al. (E896 Collaboration), Phys. Rev. Lett. **88**, 062301 (2002).
We use the 4π extrapolation given in: F. Becattini et al., Phys. Rev. C **69**, 024905 (2004).
[36] B. B. Back et al. (E917 Collaboration), Phys. Rev. Lett. **87**, 242301 (2001).
[37] C. Adler et al. (STAR Collaboration), Phys. Rev. Lett. **89**, 092301 (2002).
[38] J. Adams et al. (STAR Collaboration), Phys. Rev. Lett. **92**, 182301 (2004).
[39] K. Adcox et al. (PHENIX Collaboration), Phys. Rev. Lett. **89**, 092302 (2002).
[40] F. Kramer, C. Strabel, and M. Gaździcki, arXiv:nucl-ex/0509035.
[41] M. Bleicher et al., J. Phys. G **25**, 1859 (1999), and private communication.
[42] E. L. Bratkovskaya et al., Phys. Rev. C **69**, 054907 (2004).
[43] C. Blume (for the NA49 Collaboration), J. Phys. G **34**, S951 (2007).
[44] H. Appelshäuser et al. (NA49 Collaboration), Phys. Rev. Lett. **82**, 2471 (1999).
[45] S. Ahmad et al. (E891 Collaboration), Phys. Lett. B **382**, 35 (1996).
S. Ahmad et al., Nucl. Phys. A **636**, 507 (1998).
[46] J. Adams et al. (STAR Collaboration), Phys. Rev. Lett. **98**, 062301 (2007).
[47] C. Alt et al. (NA49 Collaboration), Phys. Rev. C **73**, 044910 (2006).
[48] M. Kaneta et al. (NA44 Collaboration), J. Phys. G **23**, 1865 (1997).
[49] L. Ahle et al. (E802 Collaboration), Phys. Rev. Lett. **81**, 2650 (1998).
[50] C. Adler et al. (STAR Collaboration), Phys. Rev. Lett. **86**, 4778 (2001).
[51] J. Adams et al. (STAR Collaboration), Phys. Rev. Lett. **92**, 112301 (2004).
[52] K. Adcox et al. (PHENIX Collaboration), Phys. Rev. C **69**, 024904 (2004).
[53] W. Cassing and E. L. Bratkovskaya, Phys. Rep. **308**, 65

(1999).
[54] J. L. Klay et al. (E895 Collaboration), Phys. Rev. C **68**, 054905 (2003).
[55] L. Ahle et al. (E802 Collaboration), Phys. Rev. C **57**, R466 (1998).
[56] C. Adler et al. (STAR Collaboration), Phys. Lett. B **595**, 143 (2004).
[57] J. Adams et al. (STAR Collaboration), Phys. Rev. Lett. **92**, 112301 (2004).
[58] K. Adcox et al. (PHENIX Collaboration), Phys. Rev. Lett. **88**, 242301 (2002).
[59] A. Andronic, P. Braun-Munzinger, and J. Stachel, Nucl. Phys. A **772**, 167 (2006).
[60] M. Gaździcki and D. Röhrich, Z. Phys. C **65**, 215 (1995).
[61] M. Gaździcki and D. Röhrich, Z. Phys. C **71**, 55 (1996).
[62] H. Weber, E. L. Bratkovskaya, W. Cassing, and H. Stöcker, Phys. Rev. C **67**, 014904 (2003).
[63] J. Cleymans, H. Oeschler, K. Redlich, S. Wheaton, Eur. Phys. J. A **29**, 119 (2006).
[64] The NA57 yields have been scaled by the corresponding number of wounded nucleons to correct for the slightly different centrality selection compared to NA49.
[65] The NA57 yields are normalized to the corresponding NA49 pion measurements.